Original article

Synergistic response of PEG coated manganese dioxide nanoparticles conjugated with doxorubicin for breast cancer treatment and MRI application

Muhammad Asif [a,*], M. Fakhar-e-Alam [a,*], Mudassir Hassan [b], Hassan Sardar [a], M. Zulqarnian [a], Li Li [c,**], Asma A. Alothman [d], Asma B. Alangary [d], Saikh Mohammad [d]

[a] *Department of Physics, Government College University Faisalabad, 38000, Pakistan*
[b] *Department of Zoology, Government College University Faisalabad, 38000, Pakistan*
[c] *Australian Institute for Bioengineering and Nanotechnology, The University of Queensland, St Lucia, Queensland 4072, Australia*
[d] *Department of Chemistry, College of Science, King Saud University, Riyadh 11451, Saudi Arabia*

ARTICLE INFO

ABSTRACT

In this research work, we designed a smart biodegradable PEG-coated MnO$_2$ nanoparticles conjugated with doxorubicin (PMnO$_2$-Dox NPs) for dual chemo-photodynamic therapy and magnetic resonance imaging (MRI) application. This highly sensitive pH-responsive PMnO$_2$-Dox NPs causes effective drug release under acidic pH environment. PMnO$_2$-Dox NPs not only improves the efficacy of chemo-photodynamic therapy due to synergistic response as well as improved MRI imaging via boosting T$_1$ MRI contrast. Manifold characterization techniques have been employed for materials investigation. Crystallography of PMnO$_2$-Dox NPs were performed by using XRD analysis, which confirmed tetragonal crystal structure with an approximate crystallite size of 20–30 nm. Surface morphology was confirmed via SEM analysis, results indicated the spherical and asymmetric agglomerated nanocluster of PMnO$_2$-Dox NPs. In *in vitro* bioassay, the anticancer activity of PMnO$_2$-Dox NPs were tested against breast cancer (MCF-7) cell line using MTT test. Moreover, it can also inhibit the growth of primary and secondary cancers without light exposure. Results suggested that PMnO$_2$-Dox NPs not only convenient for cancer treatment via combined chemo-photodynamic therapy but also address the way towards a comprehensive strategy for MRI application via bright contrast agent T1 after overcoming the problem of multidrug resistance (MDR) and synergistic response of therapeutic analysis.

1. Introduction

According to the World Health Organization (WHO) report in 2020, cancer is the second leading cause of death in the world and accounts for 10 million deaths (Sung et al., 2020; Asif et al., 2024). Among them, breast cancer is one of the most prevalent cancers with high mortality (Mohebian et al., 2021; Mettlin, 1999). Breast cancer has a high incidence and mortality rate in Pakistan (one in nine) (Khan et al., 2021). Conventional cancer treatments have been effective in defeating tumors, including surgery, photodynamic therapy (PDT), chemodynamic therapy (CDT), and radiotherapy (RT) (Wu et al., 2019; Bi et al., 2019; Sun et al., 2023). PDT has a non-invasive and remarkable anticancer efficiency (i.e., due to its abundant production of reactive oxygen species

(ROS) to kill cancer cells) and minimal side effects as compared to CDT (Zhang et al., 2020). Most importantly, the significant effect of photodynamic therapy could be enhanced by suitable laser irradiation to versatile MnO$_2$ NPs (Zhang et al., 2020).

Among the various types of nanoparticles, magnetic nanoparticles (MNPs) have received high scientific attention due to their potential applications in various fields, particularly in the medical field (Tatarchuk et al., 2017; Gao et al., 2019; Fakhar-e-Alam et al. 2024; Zhao et al., 2014; Chen et al., 2014). In the past two decades, MNPs, such as MnO$_2$ NPs have catch up much attention in biomedical applications including PDT, chemo-photodynamic therapy, hyperthermia therapy, radiotherapy, MRI guided synergetic photothermal therapy, drug delivery, bio-imaging and MRI contrast enhancement due to their unique

physio-chemical and biological properties (Li et al., 2024; Deng et al., 2011; Li et al., 2018; Luong et al., 2011; Daou et al., 2006; Sun et al., 2004).

Recent literature reports that MnO_2 NPs have been extensively studied as O_2 deliver candidate because of their exceptional physio-chemical and biological properties, and highly sensitive to Hydrogen ion (H^+) and hydrogen peroxide (H_2O_2), which are rich in tumors (Fatima, 2024; Maity et al., 2009; Faraji et al., 2010; Soon et al., 2007). Importantly, MnO_2 nanostructure can react with intracellular Glutathione (GSH) to decrease its level and increase the efficiency of PDT (Fan et al., 2016; Zhu et al., 2016; Yang et al., 2017). Furthermore, it has been demonstrated that malignant tumor cells differ from healthy cells in several specific characteristics. Conversely, tumor cells would produce excessive amounts of H_2O_2 (Kuang et al., 2011; Spyratou et al. 2012). In current, extensive literature it has been reported that mesoporous or solid MnO_2 NPs (Yang et al., 2017), core/shell MnO_2 NPs (Liang et al., 2018), and MnO_2 NSs (Zhao et al., 2014; Fan et al., 2015; Zhang et al., 2018) readily reduce in a slightly acidic behavior.

Polymer-based nanoparticles have a longer circulation time and are more stable than metal-based NPs. Polyethylene glycol (PEG) is a hydrophilic polymer that is highly biodegradable, biocompatible, stable and attractive for drug delivery due to resolving the MDR problem (Kutikov and Song, 2015; Li et al., 2023). Cheng et al. (2020) reported that Dox@H-MnO_2-PEG and Dox@H-MnO_2-FA show significant results against MRI (T_1 contrast agent) in acidic environment (Cheng et al., 2020). Hu et al. (2013) reported that PVP-coated manganese oxide nanoparticles (MnO@PVP NPs) can improve the T1 signal, used to visualize tumor images and also suggested that MnO@PVP NPs are promising candidate for enhancing T_1 MRI bright contrast agent in *in vitro* and *in vivo* (Hu et al., 2013).

In the current research work, versatile PMnO$_2$-Dox NPs were successfully synthesized and confirmed by essential characterization techniques. To overcome the MDR barrier and inhibit cancer growth by using chemo-photodynamic therapy. The PMnO$_2$-Dox NPs has been developed and applied to MCF-7 cell line. This smart study based on PMnO$_2$-Dox NPs opens new horizons for emerging cancer responsive theranostic for cancer treatment.

2. Materials and methods

2.1. Chemicals

Potassium permanganate ($KMnO_4$), sodium hydroxide (NaOH), ethanol(C_2H_6O), methanol, polyethylene glycol (PEG), 3-aminopropyl-triethoxysilane (APTES), and polyallylamine hydrochloride (PAH) were purchased from Merck (US). Doxorubicin hydrochloride ($C_{27}H_{29}NO_{11}.HCl$) was gifted from Pinum Pharmacy, Pinum Cancer Hospital Faisalabad, Punjab Medical College University, Punjab Pakistan.

2.2. Synthesis process

2.2.1. Synthesis of MnO$_2$ NPs

MnO_2 NPs were synthesized using co-precipitation approach with modified protocol (Du et al., 2023). Briefly, 0.2 M NaOH in 20 mL was added dropwise to 0.5 M $KMnO_4$ in 50 mL at vigorous stirring and then stirred for 24 h until the color turned from purple to dark brown. Finally, the prepared solution was centrifuge at 6000 rpm for 10 min and washed three times with deionized water. Finally, MnO_2 NPs were dried in the oven.

2.2.2. Synthesis of MnO$_2$-Dox

MnO_2-Dox NPs were synthesized using a slightly modified protocol as follows (Du et al., 2023): 2 mL of APTES was added to 0.1 M MnO_2 NPs in 10 mL of methanol and continuously stirred at 60 °C for 5 h. Then, the synthesized sample were washed triplet with deionized water

and dried. The aminated MnO_2 NPs has been collected. Different concentration (0–5 μg/mL) of Dox were dissolved in 3 mL methanol and 3 mg of aminated MnO_2 NPs were added to Dox methanol solution under stirring for 24 h, for each sample of Dox (Lei et al., 2021). To neutralize the HCl, triethylamine was added. Then, the prepared sample were moved to a dialysis bag for dialysis to remove unreacted Dox. The MnO_2-Dox NPs sample were collected after dried at 60 °C.

2.2.3. Synthesis of PMnO$_2$-Dox NPs

The PMnO$_2$-Dox were synthesized using filtration approach. The 0.05 g of PEG (Molecular weight (M_w) 5,000 $gmol^{-1}$) and MnO_2-Dox were dissolved in 5 mL phosphate buffered saline (PBS) and the mixture solution were squeezed 5 min and then filtered through a polycarbonate membrane filter to remove any free PEG. Finally, PEG were coated with MnO_2-Dox NPs to obtain PMnO$_2$-Dox.

2.3. Characterization of nanomaterials

Scanning electron microscope (SEM) images were measured on a "NOVA NANO SEM 430". The UV–Visible spectrophotometer was used to measure the optical density on the "BK-UV1800PC Double beam Biobase (China)". The Dox loading efficiency were determined using UV–vis at 385 and ~490 nm. Fourier transformation infrared spectroscopy (FT-IR Spectrum 2, Perkin Elmer) was utilized to identify the functional groups at the various modes. Then, the vibrating sample magnetometer (VSM) analysis were performed on "EDX model, 7200 Flagship" to determine the magnetic properties of MnO_2 NPs and PMnO$_2$-Dox NPs at room temperature. The X-ray diffraction (XRD) were performed on a "D8 advance Bruker (Germany)" to analyze the atomic structure of a crystal using Cu Kα radiation (λ = 0.154). X-ray photoelectron (XPS) were employed to further verify the formation of PMnO$_2$-Dox NPs using K-alpha X-ray photoelectron spectrophotometer "Thermo Fisher Scientific, UK". Dynamic light scattering (DLS) were performed to determine the size distribution profile of small particles in suspension using Zetasizer Nano ZS "Malvern Instruments Ltd". Finally, flow cytometry were employed on "Agilent Biosciences Inc., Santa Clara, CA" to detect cell apoptosis.

The crystallite size were calculated based on XRD using the Scherer's equation.

$$Crystallite\ size = \frac{k\lambda}{\beta cos\theta} \tag{1}$$

where k is a shape factor constant number (k = 0.98), λ is an X-ray wavelength (0.154 nm), θ is Bragg angle and β is peak width of FWHM (Full wave half maxima).

2.4. Cell culture

Human breast cancer (MCF-7) cell lines were gifted from the National Institute of Biotechnology and Genetic Engineering (NIBGE) Faisalabad, Pakistan. MCF-7 cells were cultured in Dulbecco's modified Eagle's medium (DMEM) with 10 % fetal bovine serum (FBS) and 1 % antibiotics (streptomycin, 100 μ/mL + penicillin) at 37 °C with 5 % carbon dioxide (CO_2) in a humidified incubator and for more information see our published articles (Tahir et al., 2024).

2.5. Cell viability assay

The MTT assay were used to calculate the anticancer activity of the samples on MCF-7 cell line. The MCF-7 cells were seeded in 96-microwell plates at a density of 5×10^3 cells/well and incubated overnight at 37 °C. Then, fresh mediums containing Dox in the concentration range (0, 0.5, 1, 2, 3, 4, and 5 μg/mL), MnO_2 NPs, Dox, and PMnO$_2$-Dox NPs in the concentration range (6.25, 12.5, 25, 50, 100 and 200 μg/mL) were added to the cells and incubated for 48 h. After 48 h, the cells were

washed with PBS three times and fresh mediums were added and incubated at 37 °C with 20 μL of MTT for 4 h, following with 100 μL of DMSO addition. The cell intensities were determined at wavelength of 385 and ~490 nm via Bio Base microplate reader. This study was performed three times. The % cell viability was calculated using the following equation.

$$(\%) \ CellViability = \frac{As}{Ac} \times 100 \ (\%) \tag{2}$$

Where, A_s represents the absorbance of the cells treated with the MnO$_2$ NPs and PMnO$_2$-Dox NPs and $A_{control}$ represents the absorbance of the cells cultured in DMEM.

2.6. Quantitative analysis of apoptosis via flow cytometry

MCF-7 cells were seeded in 96-microwell plates overnight at 37 °C. After that, MnO$_2$ NPs and PMnO$_2$-Dox NPs (containing 5 μg/mL Dox) were added to the cells and incubated for 48 h. After 48 h, the cells were washed with PBS, resuspended in 100 μL of binding buffer, and then stained with 5 μL of Annexin V-FITC and 7-AAD. The cells were incubated in the dark for 20 min. Finally, flow cytometry were employed to detect cell apoptosis.

2.7. Dox loading efficiency and capacity

Dox was conjugated into the PMnO$_2$ NPs. For Dox loading, PMnO$_2$ NPs was mixed with different concentrations (0–5 μg/mL) of Dox in the dark overnight. The loading efficiency of DOX increased proportionally with the amount of added doxorubicin, attaining a maximum level of 86.17 %. Finally, the PMnO$_2$-Dox NPs were attained by centrifugation (8000 rpm, 10 min), rapidly washed with water to remove the adsorbed Dox, and then dried at room temperature. The achieved PMnO$_2$-Dox NPs were used for chemo-photodynamic therapy.

The following equations were used to calculate the Dox efficiency and capacity.

$$(\%) \ Dox \ loading \ efficiency = \frac{Mass \ of \ the \ Dox \ loaded}{Initial \ mass \ of \ the \ Dox} \times 100 \ (\%) \tag{3}$$

$$(\%) \ Capacity = \frac{Mass \ of \ the \ Dox \ in \ PMnO_2 - Dox \ NPs}{Mass \ of \ PMnO_2 - Dox \ NPs} \times 100 \ (\%) \tag{4}$$

2.8. Dox release from PMnO$_2$-Dox NPs

The kinetics of drug release from PMnO$_2$-Dox NPs surfaces were studied at pH 5.5, 6.5 and 7.4. for drug release experiment, the different concentration of (0–200 μm) PMnO$_2$-Dox NPs were dispersed into 5 mL PBS, then they were stunned and irradiated with or without laser light (dose 80 j/cm^2) for 5 min in a certain period. The UV–visible spectrometer was used to measure the drug released.

2.9. Photodynamic performance

MCF-7 cell line were used to study the effects of PDT while applying parameters, 0–200 μg/mL, and light dose 80 j/cm^2 as optimum light towards MCF-7 cell model. For the *in vitro* cell apoptotic induction experiment, A semiconductor diode laser (visible blue light – 440/480 nm range, Starlight pro, Mectron Italy) with a wavelength of 480 nm was used to irradiate/expose the MCF-7 cells through the luminescent bottom of the plate. A fibre-optic (BIOSPEC, TF-D, Russia) was used to transmit the laser beam into the cells in a 6 mm diameter well (area of 0.294 cm). Drug light interval (DLI) for PMnO$_2$-Dox NPs uptake cells was half an hour. The morphology of the treated cells was observed by confocal laser scanning microscopy (CLSM). All PDT protocols were adopted as per the recommendation of the animal ethics committee of Government College University Faisalabad (GCUF).

2.10. Chemodynamic therapy performance

MCF-7 cell line was cultured in 96 microwell plates and then incubated for 24 h under recommended protocol of animal/cell ethics committee GC University Faisalabad. After obtaining 70 % cell confluency (about 24 h culturing incubation time). MCF-7 cells were exposed with working solution of various doses of Dox, MnO$_2$ NPs and PMnO$_2$-Dox NPs. After 24 h, treated with concentrations (0–5 μg/mL) Dox, (0–200 μg/mL) concentrations of MnO$_2$ NPs and PMnO$_2$-Dox NPs. Drug interval (DI) for Dox, MnO$_2$ NPs and PMnO$_2$-Dox NPs uptake cells was incubated for 48 h. The morphology of the treated cell was observed by electron microscopy (EM).

2.11. MRI bright (T1) contrast agent

The magnetic properties of MnO$_2$ NPs and PMnO$_2$-Dox NPs were characterized by MRI analysis on "MRI SIGNA" Scanner using 7 Tesla with gradients (450/675 mT/m; relaxation time 3400–4500 T/m/s; echo time 140 μs) were used as standard. MnO$_2$ NPs and PMnO$_2$-Dox NPs in the range of 0–1.0 mM were measured. The relaxations enhancement with varying TR (repetition time), and multi-slice multi-echo (MSME) were applied to estimate T_1 and T_2 respectively. Same procedure was adopted by our previous published article (Tahir et al., 2024). The algorithm creates a T1 map and extracts the MRI images, displayed high contrast as a bright signal. The tests were performed on equipment at Pinum Cancer Hospital, Punjab Medical College University, Faisalabad, Punjab, Pakistan.

2.12. Statistical analysis

The statistical analysis were performed using GraphPad Prism (version 8.0), with results reported as mean ± SD. As the values of P ≤ 0.05 were considered statistically significant (denoted by *) and the values of P ≤ 0.01 were considered highly statistically significant (denoted by **).

3. Results and discussion

3.1. The typical features of PMnO$_2$-Dox nanomedicine

In this study, PMnO$_2$-Dox NPs were constructed through step-by-step coupling and absorption process (Fig. 1). As presented in Fig. 2, the XRD patterns of MnO$_2$ NPs and PMnO$_2$-Dox NPs presented strong and typical diffraction peaks at 28.9, 37.7, 42.6, 57.4, 62.1 and 73.1°, corresponding to (110), (101), (111), (211), (220) and (301) crystal planes, respectively. These peaks are attributed to β-MnO$_2$ with tetragonal crystal structure and space group P4$_2$/mnm (**JCPDS Card No: 024-0735**) (Mauri et al., 2020). The additional peaks at 49.8 and 70° in PMnO$_2$-Dox NPs may be attributed to polyethylene glycol. We did not observe other phases of MnO$_2$ except β-MnO$_2$, thus β-MnO$_2$ is the major phases in both MnO$_2$ NPs and PMnO$_2$-Dox NPs. Both have layered structure. The crystallite sizes of MnO$_2$ NPs and PMnO$_2$-Dox NPs were estimated to be 25–30 nm respectively, using the Scherer equation.

SEM images of MnO$_2$ NPs in Fig. 3**(a–b)** exhibited that β-MnO$_2$ exhibited the crystallite structure with the size ≈20–30 nm, similar to XRD results. Dynamic light scattering (DLS) is a surface-sensitive quantitative spectroscopic technique that were performed to determine the size distribution profile of small particles in suspension. The hydrodynamic size of MnO$_2$ NPs and PMnO$_2$-Dox NPs were measured using DLS analysis. As presented in Fig. 3**(c–d),** the average size of the nanoparticles was approximately 26.31 ± 0.5 and 29.53 ± 0.67 nm.

The FTIR spectra of β-MnO$_2$ and PMnO$_2$-Dox NPs were displayed in Fig. 4**.** The significant absorption bands at 492 and 520 cm^{-1} were attributed to Mn-O stretching vibrations in MnO$_6$ octahedral in β-MnO$_2$. Compared to β-MnO$_2$, PMnO$_2$-Dox NPs in Fig. 4 showed several new peaks at 1500–2000 cm^{-1}. The absorption peak around ~1680 and
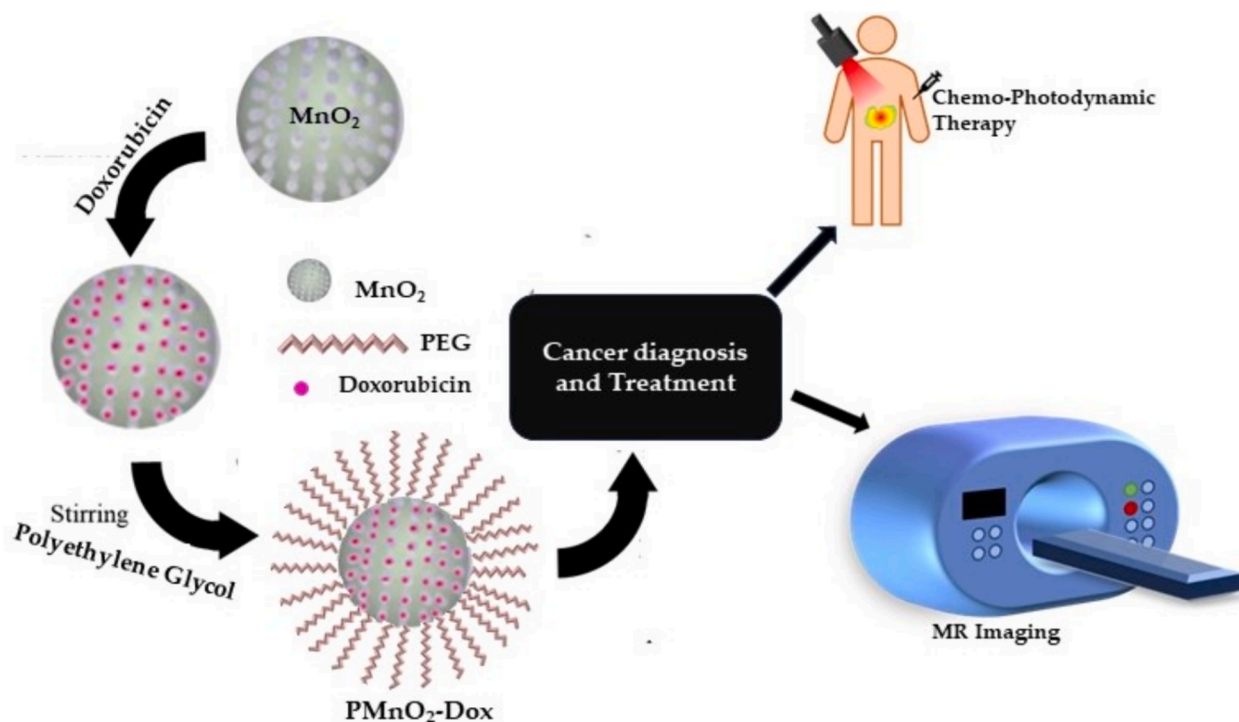
Fig. 1. Schematic diagram of synthesis, chemo-photodynamic therapy and MRI application.
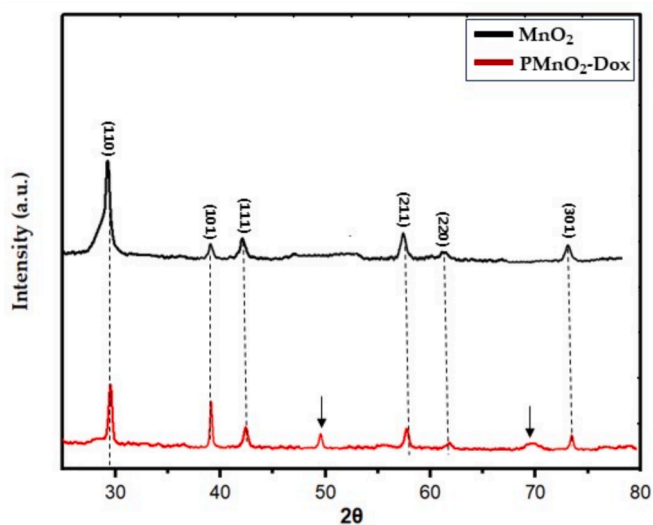
Fig. 2. The XRD pattern of MnO$_2$ NPs and PMnO$_2$-Dox NPs.

~1550 cm^{-1} were attributed to amide I and II bands, respectively, indicating the presence of Dox in MnO$_2$ NPs. The broad absorption peaks around 3000–3500 cm^{-1} can be assigned to O—H and N—H stretching vibrations from PEG and Dox, demonstrating that Dox and PEG have been conjugated onto MnO$_2$ NPs.

The UV–Visible test was performed to examine the absorption spectra of free Dox, MnO$_2$ NPs and PMnO$_2$ NPs shown in Fig. 5. The appearance of characteristic UV–Visible absorption features of Dox and MnO$_2$ NPs in the range of 480 nm and ~350–600 nm (i.e., due to the d-d transition of the Mn ion in the tetrahedral structure), respectively indicates the successful loading of Dox in the PMnO$_2$ NPs, As shown in Fig. 5 which are well matched to reported article (Yang et al., 2017).

X-ray photoelectron spectroscopy (XPS) were used to confirm the formation of PMnO$_2$-Dox NPs. The XPS spectrum showed two distinct peaks at binding energy 643.1 and 654.8 eV which correspond to the Mn$_{2p3/2}$ and Mn$_{2p1/2}$ spin–orbit peaks of MnO$_2$ NPs with an average binding energy of $\Delta E = 11.7$ eV, thereby evidencing the successful formation of MnO$_2$ NPs, as shown in Fig. 6(a). The morphology of PMnO$_2$-Dox NPs remained significantly unchanged in a pH 7.4 solution over a period of 3 days, signifying that PMnO$_2$-Dox NPs were stable in a neutral environment. In contrast, PMnO$_2$-Dox NPs displayed a time-dependent degradation pattern in acidic solutions, attributed to the breakdown of MnO$_2$ into Mn^{2+} ions. The degradation rates were quantified through the decrease in the characteristic absorbance band of MnO$_2$ NPs, as shown in Fig. 6(b). This absorbance band remained stable at pH 7.4 but showed a rapid decline at pH levels of 6.5 and 5.5, thereby further confirming the highly sensitive pH-responsive degradation pattern of PMnO$_2$-Dox NPs.

3.2. Vibrating sample magnetometer (VSM) analysis

Fig. 7 presented the hysteresis loops of β-MnO$_2$ and PMnO$_2$-Dox NPs. β-MnO$_2$ and PMnO$_2$-Dox NPs presented an S-shaped hysteresis loop with negligible remanence and coercivity, indictive of superparamagnetic nature (Chen et al., 2013; Yang et al., 2017; Ziyaee et al., 2023). VSM data exhibited that the magnetic saturation of PMnO$_2$-Dox NPs is lower than that of β-MnO$_2$, attributed to the presence of the non-magnetic PEG and Dox on the surface of β-MnO$_2$. Though slightly reduced magnetism of the PMnO$_2$-Dox NPs, the superparamagnetic properties of β-MnO$_2$ and PMnO$_2$-Dox NPs make them ideal MRI contrast agents for diagnosis, imaging, and magnetic drug delivery and hyperthermia applications.

3.3. Prevention and control of Dox release from PMnO$_2$-Dox

Doxorubicin is a clinically approved anticancer drug, which may be loaded into PMnO$_2$-Dox NPs via stirring. As depicted in demonstrated in Fig. 8, the release of Dox was superficial upto 48 h of time of incubation at pH 7.4 due to neutral pH environment base surrounding, but remarkable Dox release trend was noticed in acidic environment (pH 5.5, and 6.5). It has been seen formation of ions and the scarcity of H-bonding between doxorubicin and core shell nanomaterials of MnO$_2$ NPs
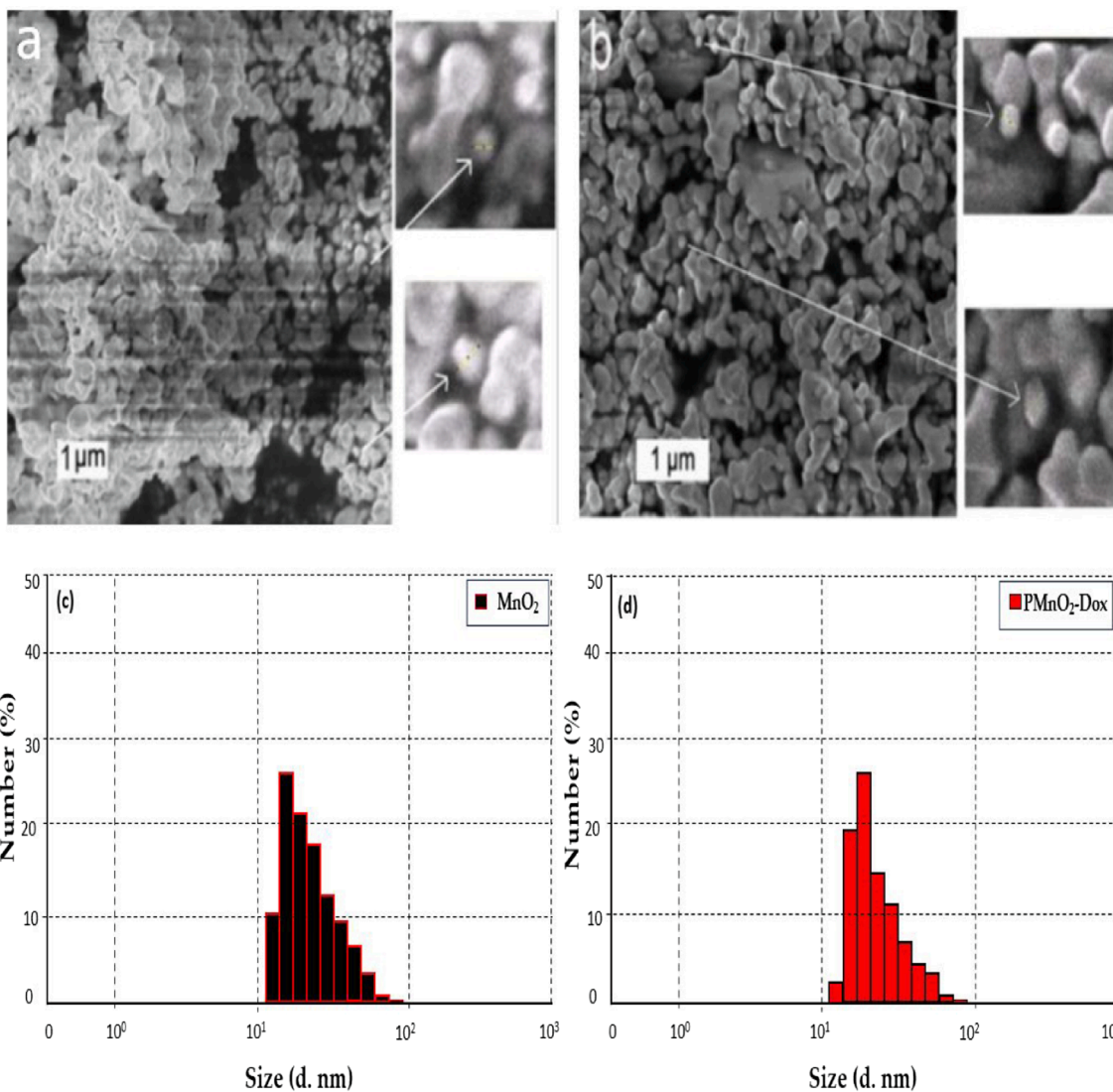
Fig. 3. The SEM images **(a–b)** of MnO_2 NPs and $PMnO_2$-Dox NPs. The DLS images **(c–d)** of MnO_2 NPs and $PMnO_2$-Dox NPs.
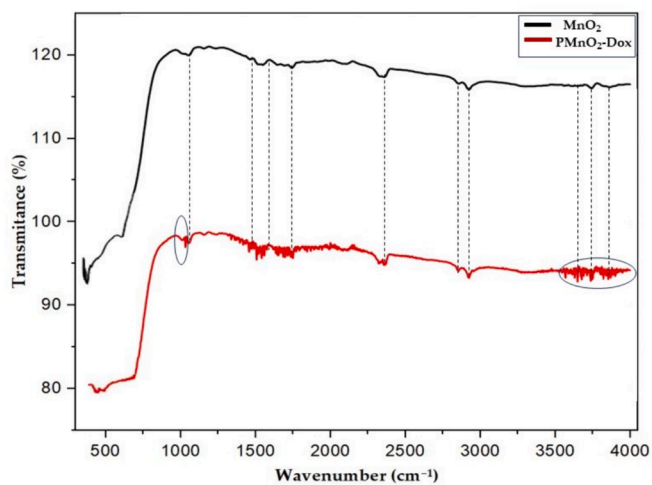
Fig. 4. FTIR of MnO_2 NPs and $PMnO_2$-Dox NPs.
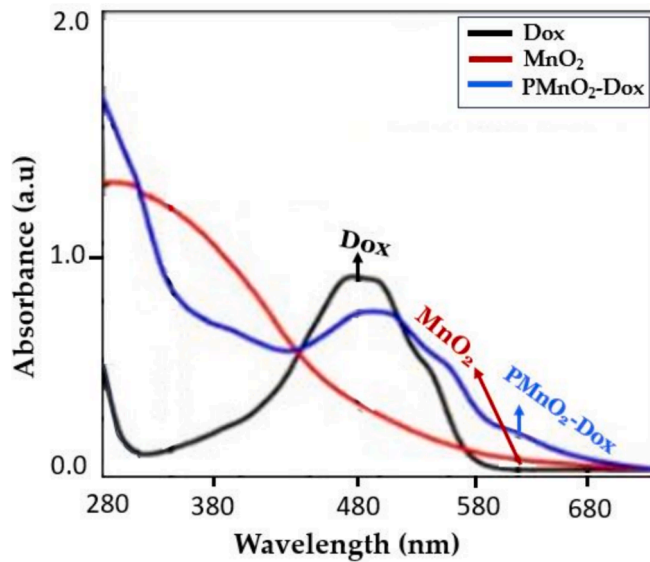
Fig. 5. UV–visible of free Dox, MnO_2 NPs and $PMnO_2$-Dox NPs.
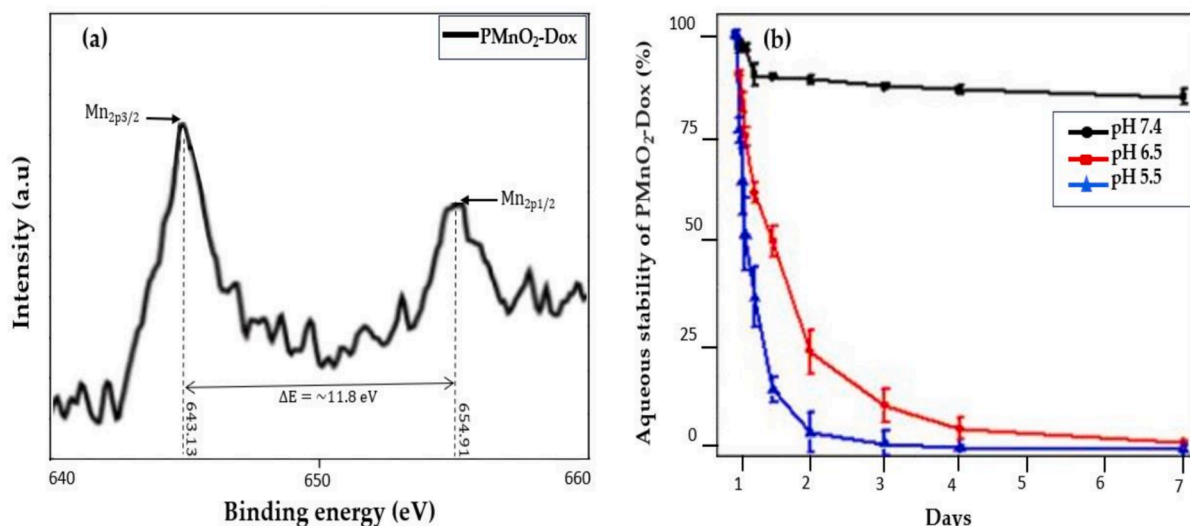
Fig. 6. (a) shows the XPS analysis and **(b)** shows the aqueous stability of PMnO$_2$-Dox NPs over a period of one week, (n = 3 ± S.D).
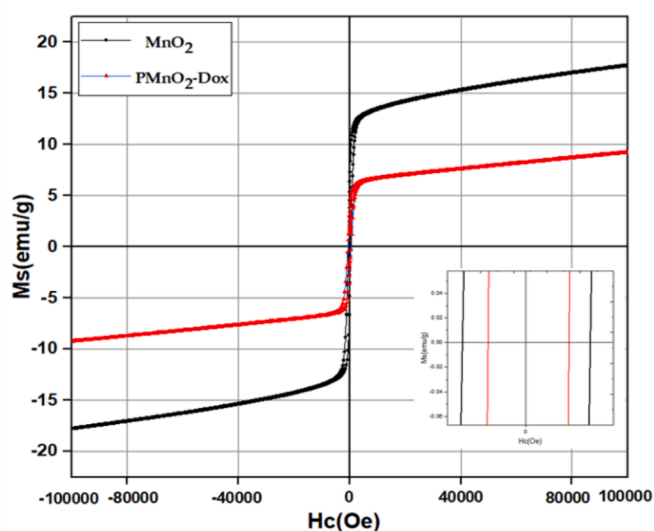
Fig. 7. Hysteresis loops of MnO$_2$ NPs and PMnO$_2$-Dox NPs.

due to thermal temperature and acidic body environment (Choi et al., 2013). In addition, significant amount of PMnO$_2$-Dox NPs accumulation towards cancerous sites due to low density lipoproteins receptor was noted as compare to healthy cells. Also, polymer coated materials were the basic requirement to overcome MDR which has been adopted in current experimental scheme. Once PMnO$_2$-Dox NPs accumulates at the cancerous site, the release rate of Dox is enhanced. The reason for this enhancement is that cancer cells have a much higher metabolic rate than healthy cells, and the cancer site becomes acidic due to the production of lactic acid. This enhancement in the release of Dox leads to the death of cancer cells through apoptosis, and some cell death attributed to necrosis. In addition, the release of Dox from PMnO$_2$-Dox NPs can be significantly enhanced by laser irradiation which may increase the entire temperature. This was ascribed to the heat produced by the photodynamic effect of MnO$_2$ NPs under visible laser irradiation to decomposition of Dox from PMnO$_2$-Dox NPs. These outcomes confirm that doxorubicin release from PMnO$_2$-Dox NPs could be triggered by the acidic environment of the cancer site and enhanced by visible laser irradiation, thereby improving the therapeutic effect (Yang et al., 2023; Ou et al., 2021).
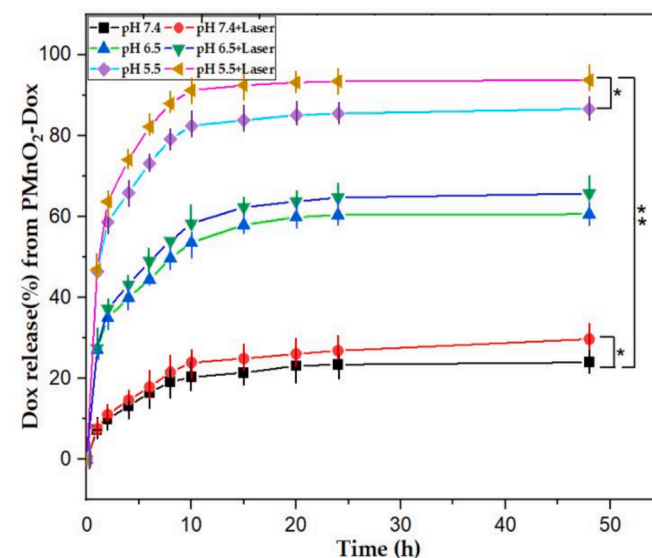
Fig. 8. The Dox release kinetic curves of PMnO$_2$-Dox NPs showing Dox release increases in acidic environment (n = 3 ± S.D), where * is significant for P ≤ 0.05 and ** is highly significant for P ≤ 0.01.

3.4. Photodynamic and chemodynamic performance

The MnO$_2$ NPs at higher concentrations exhibited slightly higher cytotoxicity towards MCF-7 cells, which may be attributed due to the Fenton reaction leading to cancer cell death (Xu et al., 2020). MCF-7 cells were exposed with doxorubicin, MnO$_2$ NPs and PMnO$_2$-Dox NPs with and without laser irradiation under recommended dose of light (80 j/cm^2) That experiments demonstrated the concentration-dependent cytotoxicity as depicted in (Fig. 9). The PMnO$_2$-Dox NPs + laser group exhibited a significant cell killing response due to photodynamic activity as compare to toxicity of MnO$_2$ NPs in the absence of light/monotherapy groups due to the synergistic treatment. After 48 h of incubation, satisfactory PDT response while using PMnO$_2$-Dox NPs with effective wavelength of laser trend depicted in (Fig. 9). In addition, Fig. 9 shows that the PMnO$_2$-Dox NPs binds to doxorubicin, indicating that doxorubicin can be successfully delivered into cancer cells for chemotherapy (Zhang et al., 2017; Hu et al., 2013). Overall results showed bare MnO$_2$ NPs, Dox and MnO$_2$ NPs with laser irradiation illustrated superficial
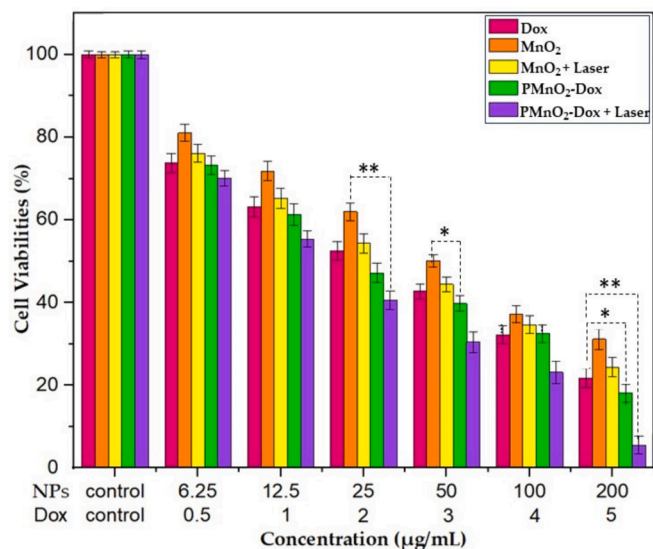
Fig. 9. Cell viabilities of MCF-7 cells treated by MnO_2 NPs and $PMnO_2$-Dox NPs with or without laser irradiation for 48 h, (n = 3 ± S.D). Laser conditions: visible blue light −440/480 nm range, Starlight pro, Mectron Italy, for 10 mins, the concentrations of MnO_2 NPs and $PMnO_2$-Dox NPs were in the range of 6.25–200 μg/mL. The Dox concentration in $PMnO_2$-Dox NPs corresponded to 5 μg/mL, where * is significant for P ≤ 0.05 and ** is highly significant for P ≤ 0.01.

response for treatment as comparison of $PMnO_2$-Dox NPs + laser group (Fig. 9). However, the $PMnO_2$-Dox NPs + laser group exhibited obvious marvelous cells death via apoptosis. These results presented that $PMnO_2$-Dox NPs + laser had significantly higher cell death due to synergistic response of chemo-photodynamic and CDT.

In this detailed discussion, Bi et al. (2019) reported that MnO_2 nanostructure can react with intracellular GSH to decrease its level and increase the efficiency of PDT and remarkable improvement in MRI images. Fan et al. (2016) reported that the nanostructure that is effectively designed inhibits the production of extracellular $^1O_2$ (singlet oxygen) by Ce6, leading to minimal side effects. Upon endocytosis, intracellular GSH degrades MnO_2 nanostructure. The nanostructure is degraded, resulting in the synchronous release of Ce6 and depletion of GSH, enabling highly efficient PDT.

3.5. Cell availability

Encouraged by their PDT and CDT performance, we evaluated the cell viability of Dox, MnO_2 NPs and $PMnO_2$-Dox NPs with or without laser irradiation on MCF-7 cells. Cell viabilities of MCF-7 cells were tested at different concentration of MnO_2 NPs and $PMnO_2$-Dox NPs (0, 6.25, 12.5, 25, 50, 100, 200 μg/mL) for 48 h. As shown in Fig. 9, all treatment groups exhibited the dose-dependent cytotoxicity against MCF-7 cells. By contrast, MnO_2 NPs slightly reduced the cell viability of MCF-7 cells under 480 nm laser irradiations, with the IC_{50} of 17.66 μg/mL. Suggesting a potential light-mediated enhancement of their therapeutic effect. Remarkably, the inclusion of Dox in MnO_2 NPs significantly enhanced the cytotoxicity of MCF-7, suggesting a potential light-mediated enhancement of their therapeutic effect, possibly through a CDT mechanism. The inclusion of Dox to $PMnO_2$ NPs significantly inhibited MCF-7 cell growth with the IC_{50} of 14.94 μg/mL due to ROS generation from CDT and interfering with DNA replication and inducing apoptosis through chemotherapy. The IC_{50} values of the DOx, MnO_2 NPs, MnO_2 NPs+ laser, $PMnO_2$-Dox NPs and $PMnO_2$-Dox NPs + laser are given in Table 1. More interestingly, the combination of $PMnO_2$ and Dox in the treatment of MCF-7 cells under laser irradiation led to most profound reduction in cell viability across all concentrations. Thus, the

Table 1
Shows the IC_{50} values of the materials.

Name of Materials	Dox	MnO_2 NPs	MnO_2 NPs + Laser	$PMnO_2$-Dox NPs	$PMnO_2$-Dox NPs+ Laser
IC_{50} Value (μg/mL)	16.70	24.05	17.66	14.94	14.15

combinational therapy of Dox with $PMnO_2$ under laser irradiation offers a multifaceted PDT/CDT/chemotherapy strategy for cancer treatment, potentially reducing associated side effects, drug resistance, and the highest therapeutic efficacy of 94.87 % was obtained at a concentration of 200 μg/mL of $PMnO_2$-Dox NPs with laser irradiation. The morphologies of MCF-7 cells treated by $PMnO_2$-Dox NPs with or without laser irradiation have been further explored. As shown in Fig. 10, cancer cell apoptosis were observed in all $PMnO_2$-Dox NPs with or without laser irradiation. As the concentrations of MnO_2 and Dox increased in the treatment, the morphology of MCF-7 cells drastically altered, leading to a drastic reduction in cell viabilities due to apoptosis, and some cell death occurs through necrosis. Under laser irradiation, more apoptosis was observed. These data were consistent with the cell viability. The increased efficiency of $PMnO_2$-Dox NPs with laser irradiation was ascribed to the synergistic effects of PDT, CDT and chemotherapy as demonstrated in Fig. 9.

Flow cytometry (FC) were employed to quantitatively measure the apoptotic impact of MnO_2 NPs and $PMnO_2$-Dox NPs. After 48 h of treatment with MnO_2 NPs, MnO_2 NPs + laser, $PMnO_2$-Dox NPs, and $PMnO_2$-Dox NPs+ laser, the apoptosis rates were determined to be 12.97 ± 1.91, 15.11 ± 1.57, 27.27 ± 2.69, and 29.75 ± 2.37 %, respectively, as shown in Fig. 11. Notably, the apoptosis rate of the $PMnO_2$-Dox NPs+ laser group was substantially greater compared to other groups.

3.6. Magnetic resonace imaging

Magnetic resonance imaging (MRI) of MnO_2 NPs and $PMnO_2$-Dox NPs incubated in PBS solution for 4 h were measured using an (MRI SIGNA) 7 T scanner. As shown in Fig. 12(a, b), the MRI bright signal enhanced with the increase of MnO_2 concentration from 0–1 mM, determining that manganese is a T_1 contrast agent. The MRI experiment was done at different concentration (0, 0.2, 0.4, 0.6, 0.8 and 1 mM). In comparison with MnO_2 NPs, and $PMnO_2$-Dox NPs exhibited reduced T_1 relaxation and significantly enhanced signal intensity in T_1-weighted images. *In vitro* and in vivo, these magnetic MnO_2 NPs and $PMnO_2$-Dox NPs offer marvelous T1 bright contrast agents for MRI due to the decomposition of MnO_2 or induced of Mn^{2+} ion under acidic condition. In the current study, MnO_2 NPs exhibits less brightness than $PMnO_2$-Dox NPs. Hence, $PMnO_2$-Dox NPs can be applied as a T1 bright contrast agent for efficient outcomes. Furthermore, the $PMnO_2$-Dox NPs were employed to calculate the r1 relaxivities under the basic to acidic condition. It can be noted that under varying pHs (7.4, 6.5 and 5.5 pH) conditions, the value of r1 remarkably increased from very first value 0.049–8.97 $mM^{-1}S^{-1}$ after incubation in 5.5 pH PBS for 4 h, shown in Fig. 12(c). In this discussion, Hu et al. (2013) reported that PVP-coated manganese oxide nanoparticles (MnO@PVP NPs) can improve the T1 signal and utilized to visualize tumor images. *In vitro* and *in vivo* analysis of MnO@PVP NPs proposed that are promising candidate for MRI T1 bright contrast agents.

4. Conclusions

The developed $PMnO_2$-Dox NPs for improved chemo-photodynamic therapy and MRI application. Crystallography of $PMnO_2$-Dox were employed by using XRD analysis, which confirmed tetragonal crystal structure. Surface morphology was confirmed via SEM analysis, results indicated the spherical and asymmetric agglomerated nanocluster of $PMnO_2$-Dox NPs. The functional groups and magnetization were
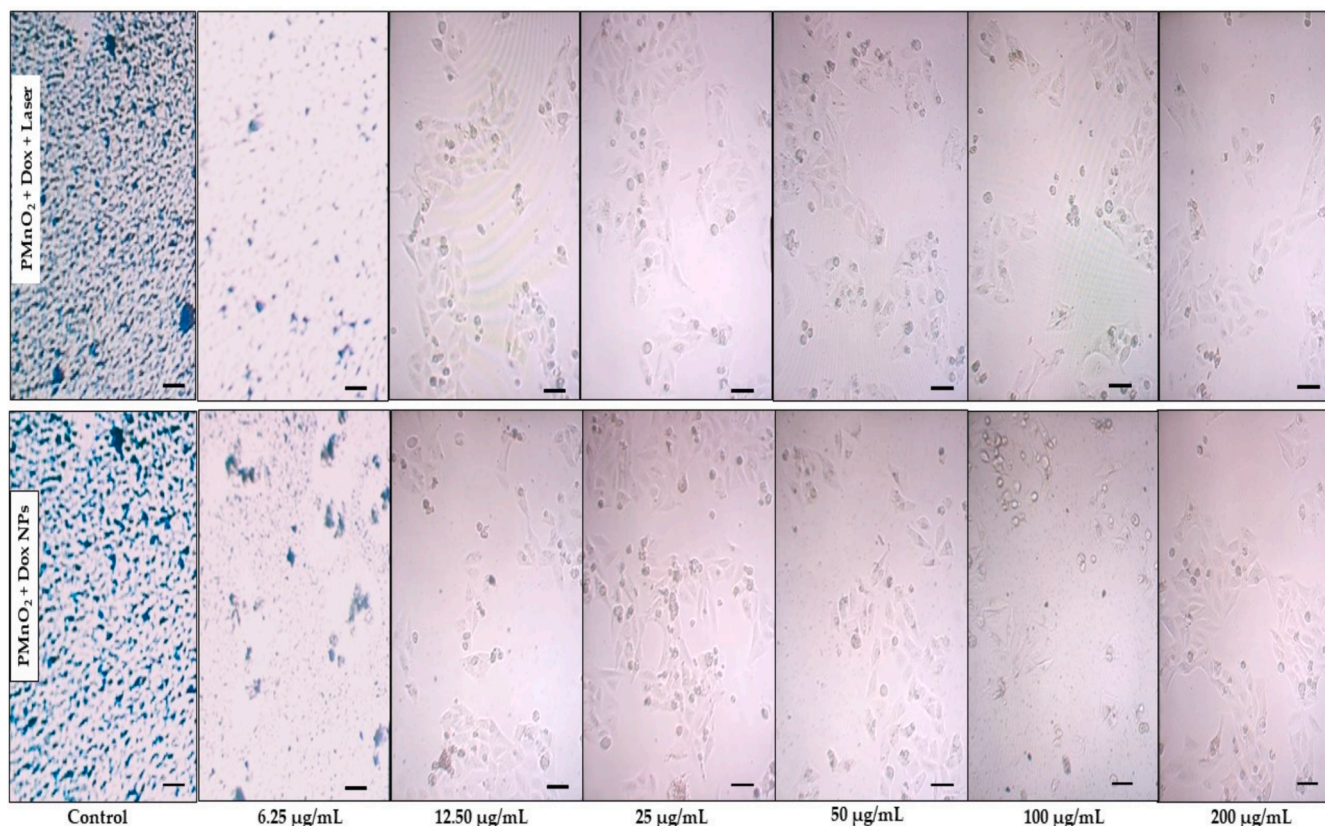
Fig. 10. Morphological and apoptotic analysis of MCF-7 cells treated by PMnO$_2$-Dox NPs with and without laser irradiation for 10 min. Scale bar: 100 μm for each display.
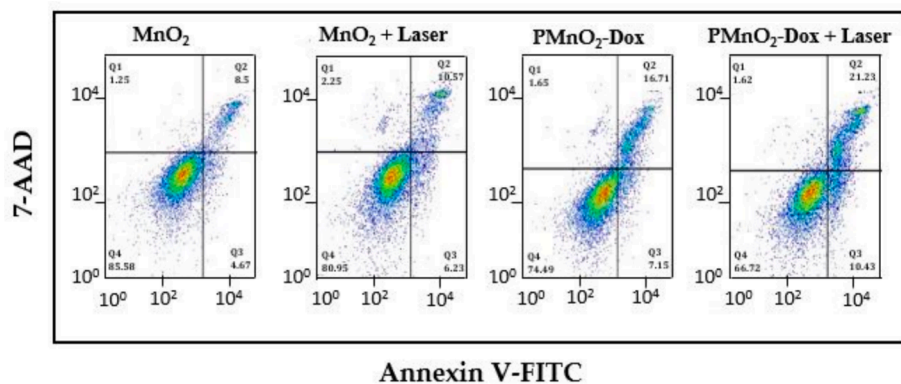
Fig. 11. Flow cytometry analysis of MnO$_2$ NPs and PMnO$_2$-Dox NPs with and without laser irradiation revealed the apoptosis ratio.

confirmed using FTIR and VSM analysis, respectively. MnO$_2$ NPs provided PDT upon laser irradiation, doxorubicin certainly release at the cancer site for chemotherapy due to laser irradiation and pH value reduction of PMnO$_2$-Dox NPs. Associated with previously described MnO$_2$ NPs and PMnO$_2$-Dox NPs exhibits efficient drug loading and release rewards. This highly sensitive pH-responsive of PMnO$_2$-Dox NPs causes effective drug release under acidic pH environment. PMnO$_2$-Dox NPs not only improves the efficacy of chemo-photodynamic therapy due to synergistic response as well as improved MRI imaging via boosting T$_1$ MRI contrast. In addition, it can also inhibit the growth of primary and secondary cancers without light exposure. On the basis of results, it is concluded that PMnO$_2$-Dox NPs not only convenient for cancer treatment via chemo-photodynamic therapy but also address the way towards a comprehensive strategy for MRI application via bright contrast agent T1 after overcoming the problem of MDR and synergistic response

of therapeutic analysis.

CRediT authorship contribution statement

Muhammad Asif: Conceptualization, Data curation, Writing – original draft, Methodology, Software, Investigation, Validation, Supervision, Project administration. **M. Fakhar-e-Alam:** Conceptualization, Investigation, Validation, Supervision, Project administration, Writing – review & editing. **Mudassir Hassan:** Formal analysis, Visualization, Methodology, Resources. **Hassan Sardar:** Methodology, Resources, Formal analysis. **M. Zulqarnian:** Software, Resources, Formal analysis. **Li Li:** Formal analysis, Investigation, Resources, Validation, Visualization, Writing – review & editing. **Asma A. Alothman:** Formal analysis, Funding acquisition, Resources, Visualization. **Asma B. Alangary:** Formal analysis, Funding acquisition, Resources, Visualization.
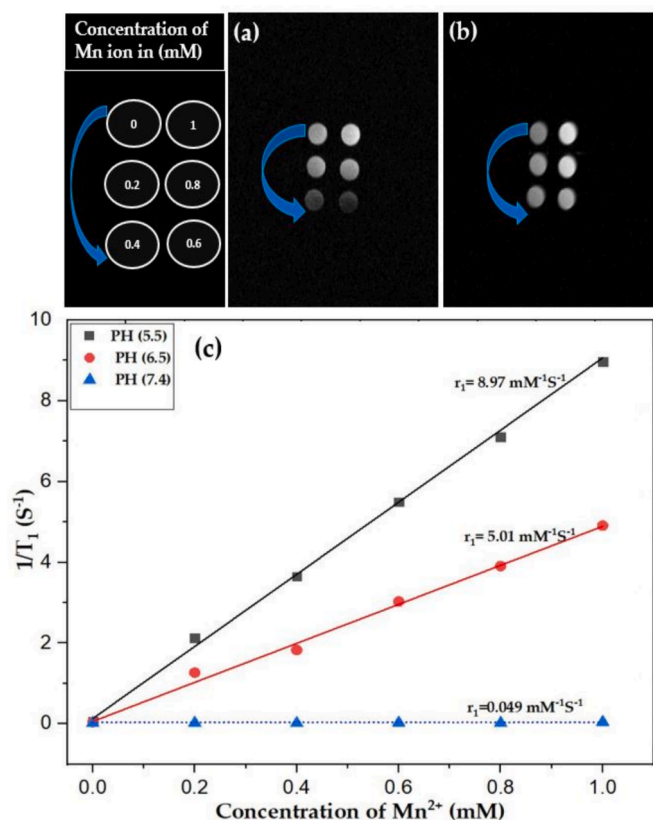
Fig. 12. **(a–b)** shows the MRI images of MnO_2 NPs and $PMnO_2$-Dox NPs at different concentration (0, 0.2, 0.4, 0.6, 0.8 and 1 mM) and **(c)** shows the r_1 relativities for $PMnO_2$-Dox NPs were 0.049, 5.01 and 8.97 $mM^{-1}S^{-1}$ at 7.4, 6.5 and 5.5 pH, respectively, (n = 3 ± S.D).

Saikh Mohammad: Formal analysis, Funding acquisition, Resources, Visualization.

Declaration of competing interest

The authors declare that they have no known competing financial interests or personal relationships that could have appeared to influence the work reported in this paper.

Acknowledgment

References

Asif, M., Iqbal, W., Fakhar-e-Alam, M., Hussain, Z., Saadullah, M., Hassan, M., Al-Qahtani, N.H., 2024. Synthesis and characterization of chemically and green-synthesized silver oxide particles for evaluation of antiviral and anticancer activity. Pharmaceuticals 17 (7), 908.

Bi, H., Dai, Y., Yang, P., Xu, J., Yang, D., Gai, S., Lin, J., 2019a. Glutathione and H2O2 consumption promoted photodynamic and chemotherapy based on biodegradable MnO2–Pt@ Au25 nanosheets. Chem. Eng. J. 356, 543–553.

Bi, H., Dai, Y., Yang, P., Xu, J., Yang, D., Gai, S., He, F., An, G., Zhong, C., Lin, J., 2019b. Glutathione and H2O2 consumption promoted photodynamic and chemotherapy based on biodegradable MnO2–Pt@Au25 nanosheets. Chem. Eng. J. 356, 543–553. https://doi.org/10.1016/J.CEJ.2018.09.076.

Chen, K., Dong Noh, Y., Li, K., Komarneni, S., Xue, D., 2013. Microwave-hydrothermal crystallization of polymorphic MnO2 for electrochemical energy storage. J. Phys. Chem. C 117, 10770–10779.

Chen, Y., Ye, D., Wu, M., Chen, H., Zhang, L., Shi, J., Wang, L., 2014. Break-up of two-dimensional MnO2 nanosheets promotes ultrasensitive pH-triggered theranostics of cancer. Adv. Mater. 26, 7019–7026. https://doi.org/10.1002/ADMA.201402572.

Cheng, M., Yu, Y., Huang, W., Fang, M., Chen, Y., Wang, C., Cai, W., Zhang, S., Wang, W., Yan, W., 2020. Monodisperse hollow MnO2 with biodegradability for efficient targeted drug delivery. ACS Biomater. Sci. Eng. 6, 4985–4992.

Choi, S.Y.C., Collins, C.C., Gout, P.W., Wang, Y., 2013. Cancer-generated lactic acid: a regulatory, immunosuppressive metabolite? J Pathol. 230, 350–355.

Daou, T.J., Pourroy, G., Bégin-Colin, S., Grenèche, J.M., Ulhaq-Bouillet, C., Legaré, P., Bernhardt, P., Leuvrey, C., Rogez, G., 2006. Hydrothermal synthesis of monodisperse magnetite nanoparticles. Chem. Mater. 18, 4399–4404. https://doi.org/10.1021/CM060805R/ASSET/IMAGES/MEDIUM/CM060805RN00001.

Deng, R., Xie, X., Vendrell, M., Chang, Y.T., Liu, X., 2011. Intracellular glutathione detection using MnO2-nanosheet-modified upconversion nanoparticles. J. Am. Chem. Soc. 133, 20168–20171. https://doi.org/10.1021/JA2100774/SUPPL_FILE/JA2100774_SI_001.PDF.

Du, J., Sun, J., Liu, X., Wu, Q., Shen, W., Gao, Y., Liu, Y., Wu, C., 2023. Preparation of C6 cell membrane-coated doxorubicin conjugated manganese dioxide nanoparticles and its targeted therapy application in glioma. Eur. J. Pharm. Sci. 180, 106338.

Fakhar-e-Alam, M., Amjad, I., Saadullah, M., Tahir, M., Jawad, M., Asif, M., Rashad, M., 2024. Antitumor activity of zinc oxide nanoparticles fused with green extract of Nigella sativa. J. Saudi Chem. Soc. 28 (2), 101814.

Fan, W., Bu, W., Shen, B., He, Q., Cui, Z., Liu, Y., Zheng, X., Zhao, K., Shi, J., 2015. Intelligent MnO2 nanosheets anchored with upconversion nanoprobes for concurrent pH-/H2O2-responsive UCL imaging and oxygen-elevated synergetic therapy. Adv. Mater. 27, 4155–4161. https://doi.org/10.1002/ADMA.201405141.

Fan, H., Yan, G., Zhao, Z., Hu, X., Zhang, W., Liu, H., Fu, X., Fu, T., Zhang, X.B., Tan, W., 2016. A smart photosensitizer-manganese dioxide nanosystem for enhanced photodynamic therapy by reducing glutathione levels in cancer cells. Angew. Chem. Int. Ed. 55, 5477–5482.

Faraji, M., Yamini, Y., Rezaee, M., 2010. Magnetic nanoparticles: synthesis, stabilization, functionalization, characterization, and applications. J. Iran. Chem. Soc. 7, 1–37. https://doi.org/10.1007/BF03245856/METRICS.

Fatima, N., ul Hassan, S.M., Fakhar-e-Alam, M., Asif, M., Imtiaz, S., Anwar, S., Imran, M., 2024. Development of a novel fluorescence spectroscopy-based method using layered double hydroxides to study degradation of E. coli in water. J. Mol. Struct. 1310, 138248.

Gao, F., Tang, Y., Liu, W.L., Zou, M.Z., Huang, C., Liu, C.J., Zhang, X.Z., 2019. Intra/extracellular lactic acid exhaustion for synergistic metabolic therapy and immunotherapy of tumors. Adv. Mater. 31, 1904639 https://doi.org/10.1002/ADMA.201904639.

Gul, S., Yousuf, M.A., Anwar, A., Warsi, M.F., Agboola, P.O., Shakir, I., Shahid, M., 2020b. Al-substituted zinc spinel ferrite nanoparticles: preparation and evaluation of structural, electrical, magnetic and photocatalytic properties. Ceram. Int. 46, 14195–14205. https://doi.org/10.1016/J.CERAMINT.2020.02.228.

Hu, X., Ji, Y., Wang, M., Miao, F., Ma, H., Shen, H., Jia, N., 2013. Water-soluble and biocompatible MnO@PVP nanoparticles for MR imaging *In Vitro* and *In Vivo*. J. Biomed. Nanotechnol. 9, 976–984. https://doi.org/10.1166/JBN.2013.1602.

Khan, N.H., Duan, S.F., Wu, D.D., Ji, X.Y., 2021. Better reporting and awareness campaigns needed for breast cancer in Pakistani women. Cancer Manag. Res. 13, 2125–2129. https://doi.org/10.2147/CMAR.S270671.

Kuang, Y., Baakrishnan, K., Gandhi, V., Peng, X., 2011. Hydrogen peroxide inducible DNA cross-linking agents: targeted anticancer prodrugs. J. Am. Chem. Soc. 133, 19278–19281.

Kutikov, A.B., Song, J., 2015. Biodegradable PEG-based amphiphilic block copolymers for tissue engineering applications. ACS Biomater. Sci. Eng. 1 (7), 463–480.

Lei, M., Chen, G., Zhang, M., Lei, J., Li, T., Li, D., Zheng, H., 2021. A pH-sensitive drug delivery system based on hyaluronic acid co-deliver doxorubicin and aminoferrocene for the combined application of chemotherapy and chemodynamic therapy. Colloids Surf. B: Biointerfaces 203, 111750. https://doi.org/10.1016/J.COLSURFB.2021.111750.

Li, X., Duan, Z., Chen, X., Pan, D., Luo, Q., Gu, L., Luo, K., 2023. Impairing tumor metabolic plasticity via a stable metal-phenolic-based polymeric nanomedicine to suppress colorectal cancer. Adv. Mater. 35 (23), 2300548.

Li, H., Gong, Q., Luo, K., 2024. Biomarker-driven molecular imaging probes in radiotherapy. Theranostics 14 (10), 4127.

Li, J., Zhang, X., Zhao, M., Wu, L., Luo, K., Pu, Y., He, B., 2018. Tumor-pH-sensitive PLLA-based microsphere with acid cleavable acetal bonds on the backbone for efficient localized chemotherapy. Biomacromolecules 19 (7), 3140–3148.

Liang, R., Liu, L., He, H., Chen, Z., Han, Z., Luo, Z., Wu, Z., Zheng, M., Ma, Y., Cai, L., 2018. Oxygen-boosted immunogenic photodynamic therapy with gold nanocages@ manganese dioxide to inhibit tumor growth and metastases. Biomaterials 177, 149–160. https://doi.org/10.1016/J.BIOMATERIALS.2018.05.051.

Luong, T.T., Ha, T.P., Tran, L.D., Do, M.H., Mai, T.T., Pham, N.H., Phan, H.B.T., Pham, G.H.T., Hoang, N.M.T., Nguyen, Q.T., Nguyen, P.X., 2011. Design of carboxylated Fe3O4/poly(styrene-co-acrylic acid) ferrofluids with highly efficient magnetic heating effect. Colloids Surf. A: Physicochem. Eng. Asp. 384, 23–30.

Maity, D., Choo, S.G., Yi, J., Ding, J., Xue, J.M., 2009. Synthesis of magnetite nanoparticles via a solvent-free thermal decomposition route. J. Magn. Magn. Mater. 321, 1256–1259. https://doi.org/10.1016/J.JMMM.2008.11.013.

Mauri, M., Collico, V., Morelli, L., Das, P., García, I., Penaranda Avila, J., Bellini, M., Rotem, R., Truffi, M., Corsi, F., Simonutti, R., Liz-Marzán, L.M., Colombo, M., Prosperi, D., 2020a. MnO nanoparticles embedded in functional polymers as T1 contrast agents for magnetic resonance imaging. ACS Appl. Nano Mater. 3, 3787–3797.

Mauri, M., Collico, V., Morelli, L., Das, P., García, I., Penaranda Avila, J., Bellini, M., Rotem, R., Truffi, M., Corsi, F., Simonutti, R., Liz-Marzán, L.M., Colombo, M., Prosperi, D., 2020b. MnO nanoparticles embedded in functional polymers as T1

contrast agents for magnetic resonance imaging. ACS Appl. Nano Mater. 3, 3787–3797.

Mettlin, C., 1999. Global breast cancer mortality statistics. CA Cancer J. Clin. 49, 138–144. https://doi.org/10.3322/CANJCLIN.49.3.138.

Mohebian, Z., Babazadeh, M., Zarghami, N., Mousazadeh, H., 2021. Anticancer efficiency of curcumin-loaded mesoporous silica nanoparticles/nanofiber composites for potential postsurgical breast cancer treatment. J. Drug Del. Sci. Technol. 61, 102170.

Ou, J., Tian, H., Wu, J., Gao, J., Jiang, J., Liu, K., Wang, S., Wang, F., Tong, F., Ye, Y., Liu, L., Chen, B., Ma, X., Chen, X., Peng, F., Tu, Y., 2021. MnO2-based nanomotors with active Fenton-like Mn2+ delivery for enhanced chemodynamic therapy. ACS Appl. Mater. Interfaces 13, 38050–38060.

Soon, G.K., Piao, Y., Park, J., Angappane, S., Jo, Y., Hwang, N.M., Park, J.G., Hyeon, T., 2007. Kinetics of monodisperse iron oxide nanocrystal formation by "heating-up" process. J. Am. Chem. Soc. 129, 12571–12584.

Spyratou, E., Makropoulou, M., Mourelatou, E.A., Demetzos, C., 2012. Biophotonic techniques for manipulation and characterization of drug delivery nanosystems in cancer therapy. Cancer Lett. 327, 111–122.

Sun, L., Gao, W., Wang, J., Niu, X., Kurniawan, N., Li, L., Xu, Z.P., 2023. A new sono-chemo sensitizer overcoming tumor hypoxia for augmented sono/chemo-dynamic therapy and robust immune-activating response. Small 19.

Sun, S., Zeng, H., Robinson, D.B., Raoux, S., Rice, P.M., Wang, S.X., Li, G., 2004. Monodisperse MFe2O4 (M = Fe Co, Mn) nanoparticles. J. Am. Chem. Soc. 126, 273–279. https://doi.org/10.1021/JA0380852/SUPPL_FILE/JA0380852SI20031027_103500.PDF.

Sung, H., Ferlay, J., Siegel, R.L., Laversanne, M., Soerjomataram, I., Jemal, A., Bray, F., 2020. Global Cancer Statistics 2020: GLOBOCAN Estimates of Incidence and Mortality Worldwide for 36 Cancers in 185 Countries. CA Cancer J. Clin. 71 (2021), 209–249. https://doi.org/10.3322/CAAC.21660.

Tahir, M., Fakhar-e-Alam, M., Asif, M., Iqbal, M.J., Abbas, A., Hassan, M., Mohammad, S., 2024. Investigation of gadolinium doped manganese nano spinel ferrites via magnetic hyperthermia therapy effect towards MCF-7 breast cancer. Heliyon 10 (3), e24792.

Tatarchuk, T., Bououdina, M., Judith Vijaya, J., John Kennedy, L., 2017. Spinel ferrite nanoparticles: synthesis, crystal structure, properties, and perspective applications. Springer Proc. Phys. 195, 305–325. https://doi.org/10.1007/978-3-319-56422-7_22/COVER.

Wu, Q., Chen, G., Gong, K., Liu, X., Guo, S., Wang, F., Wang, J., Ge, X., 2019. MnO2-laden black phosphorus for MRI-guided synergistic PDT, PTT, and chemotherapy. Matter. https://doi.org/10.1016/j.matt.2019.03.007.

Xu, F., Zhu, J., Lin, L., Zhang, C., Sun, W., Fan, Y., Shi, X., 2020. Multifunctional PVCL nanogels with redox-responsiveness enable enhanced MR imaging and ultrasound-promoted tumor chemotherapy. Theranostics 10 (10), 4349.

Yang, G.B., Xu, L.G., Chao, Y., Xu, J., Sun, X.Q., Wu, Y.F., Peng, R., Liu, Z., 2017a. Hollow MnO2 as a tumor-microenvironment-responsive biodegradable nano-platform for combination therapy favoring antitumor immune responses. Nat. Commun. 8, 902.

Yang, G., Xu, L., Chao, Y., Xu, J., Sun, X., Wu, Y., Liu, Z., 2017b. Hollow MnO2 as a tumor-microenvironment-responsive biodegradable nano-platform for combination therapy favoring antitumor immune responses. Nat. Commun. 8 (1), 902.

Yang, G., Liu, J., Zhang, Z., Yuan, L., Tian, H., Yang, X., 2023. Preparation of acid-driven magnetically imprinted micromotors and selective loading of phycocyanin. J. Mater. Chem. B.

Zhang, W., Li, S., Liu, X., Yang, C., Hu, N., Dou, L., Zhao, B., Zhang, Q., Suo, Y., Wang, J., 2018. Oxygen-generating MnO2 nanodots-anchored versatile nanoplatform for combined chemo-photodynamic therapy in hypoxic cancer. Adv. Funct. Mater. 28, 1706375 https://doi.org/10.1002/ADFM.201706375.

Zhang, M., Liu, X., Luo, Q., Wang, Q., Zhao, L., Deng, G., Ge, R., Zhang, L., Hu, J., Lu, J., 2020a. Tumor environment responsive degradable CuS@mSiO2@MnO2/DOX for MRI guided synergistic chemo-photothermal therapy and chemodynamic therapy. Chem. Eng. J. 389, 124450 https://doi.org/10.1016/J.CEJ.2020.124450.

Zhang, Q., Shen, C., Zhao, N., Xu, F.J., 2017. Redox-responsive and drug-embedded silica nanoparticles with unique self-destruction features for efficient gene/drug codelivery. Adv. Funct. Mater. 27.

Zhao, Z., Fan, H., Zhou, G., Bai, H., Liang, H., Wang, R., Zhang, X., Tan, W., 2014. Activatable fluorescence/MRI bimodal platform for tumor cell imaging via MnO2 nanosheet-aptamer nanoprobe. J. Am. Chem. Soc. 136, 11220–11223. https://doi.org/10.1021/JA5029364/SUPPL_FILE/JA5029364_SI_001.PDF.

Zhu, W., Dong, Z., Fu, T., Liu, J., Chen, Q., Li, Y., Zhu, R., Xu, L., Liu, Z., 2016. Modulation of hypoxia in solid tumor microenvironment with MnO2 nanoparticles to enhance photodynamic therapy. Adv. Funct. Mater. 26, 5490–5498.

Ziyaee, S., Malekzadeh, R., Ghorbani, M., Nasiri Motlagh, B., Asghariazar, V., Mortezazadeh, T., 2023. Preparation of MnO2@poly-(DMAEMA-co-IA)-conjugated methotrexate nano-complex for MRI and radiotherapy of breast cancer application. MAGMA 36, 779–795.